A finite volume approach for general fully coupled anisotropic porous solid mechanics of fiber reinforcements in Liquid Composite Molding

Sarah Schlegel [ID] *, Florian Wittemann [ID], Luise Kärger [ID]

Karlsruhe Institute of Technology (KIT), Institute of Vehicle System Technology - Lightweight Engineering, Rintheimer Querallee 2, 76131 Karlsruhe, Germany

ARTICLE INFO

ABSTRACT

In this work, a finite volume method is developed to capture the interaction between the infiltrating resin and the deforming fiber reinforcement in liquid composite molding (LCM). The method consists of three parts: (1) the fluid flow through a porous medium, which depends on the fiber volume fraction (FVF) and the fiber orientation, (2) the solid mechanics of the porous fiber structure considering the general anisotropic material stiffness, which also depends on the FVF and the fiber orientation, and (3) an internal coupling approach to couple porous solid mechanics and fluid flow with an iterative scheme. An anisotropic model of porous solid mechanics is proposed and verified in a unidirectional case to capture fluid-induced deformations of the porous medium. In a second verification case, the stress state is verified in an open-hole tensile test against an analytical solution for different degrees of material anisotropy. Finally, the infiltration and compaction predictions of the model are validated against experimental data from the literature using a three-dimensional plate. In addition, the infiltration behavior with the anisotropic model is compared to the isotropic model to illustrate the advantage of the new approach.

1. Introduction

One important manufacturing process for high performance composites is Liquid Composite Molding (LCM), which includes Resin Transfer Molding (RTM), Wet Compression Molding (WCM), and Vacuum Assisted Resin Infusion (VARI). The trend in manufacturing is towards flexible tooling like in Compression RTM (CRTM), where a movable mold is used to reduce the infiltration pressure and time. This means that not only the resin flow through the porous medium, but also the deformation of the fiber reinforcement must be taken into account. The same applies to the manufacturing of sandwich structures with an integrated foam core, where the deforming foam must also be taken into account. In order to control these complex processes, avoid defects and keep process times short, it is useful to model the manufacturing process as accurately as possible. If the process is well understood, emissions, energy consumption and rejects can also be reduced, which is an important step towards a climate-friendly production. Therefore, in this paper a method is presented to describe anisotropic deformations of a porous medium in a finite volume framework. The aim is to be able to better predict the deformations of the fiber reinforcement and the formation of air inclusions simultaneously.

Simulations of infiltration flow in LCM manufacturing processes have been extensively studied for more than three decades to better design and understand the process [1–5]. If one domain boundary is

flexible, the mutual influence between the fluid flow, the deformation of the boundary, and the deformation of the fiber reinforcement poses a particular challenge in predicting the filling behavior. The mutual dependencies are to be reproduced in the mold filling simulation by means of fluid–structure interaction (FSI). This is the case, for example, in the VARI process [6–10] and in the processing of Sandwich components with an integrated foam core. During the processing of sandwich components the fluid pressure induces different types of deformation and displacements of the foam core, as analyzed by Al-Hamdan et al. [11], Binetruy and Advani [12]. In this context, Deleglise et al. [13] and Seuffert [14] investigated the influence of forced and induced deformations on the filling behavior and found a large influence of foam core deformations on the injection pressure and thus on the filling behavior.

In CRTM the movement of the upper mold and the resulting compression of the fiber reinforcement have to be described additionally. This induced compression poses the additional challenge of modeling the deformations of the porous medium during infiltration. A finite element approach to model the deformation of a dry fiber mat for Injection/Compression LCM was derived by Pillai et al. [15]. The model is capable of capturing complex preform shapes and allows for large deformations and a variety of constitutive equations for the behavior

---

* Corresponding author.
  E-mail address: sarah.schlegel@kit.edu (S. Schlegel).

of fiber reinforcement. However, the infiltration of the preform is not considered. Based on the work of Pillai et al. [15], Bickerton and Abdullah [16] present an experimental and numerical study on the influence of compressive force and velocity on the infiltration behavior in CRTM. They assume that the deformations are limited to the thickness direction, but allow for a three-dimensional flow field. The influence of reinforcement compaction on the infiltration flow was also studied by Bhat et al. [17] and Merotte et al. [18] in a parametric study using the finite element (FE) tool Liquid Injection Molding Simulation (LIMS) in the thickness direction. Martin et al. [19] investigated the influence of resin channels on press forces and inlet pressure, comparing experimental findings with FE simulations using 2D elements. They found that 2D elements are sufficiently accurate for their application and concluded that viscosity and permeability have a large influence on the infiltration.

If the component thickness is larger, a three-dimensional approach is required as described by Yang et al. [20] and Shojaei [21]. Shojaei [21] model the fluid flow with a control volume (CV)/FEM approach, while Yang et al. [20] use a multiphase Volume of Fluid (VOF) approach in a commercial FE tool. Both use a three-dimensional approach for the fluid flow, but model compression and stress in the porous medium only in the thickness direction. Yang et al. [20] additionally account for the initial gap as a resin channel, in which the incompressible Navier–Stokes equation is solved instead of assuming a porous medium with high permeability and porosity. Dereims et al. [22] also present a three-dimensional FE approach to couple a porous solid and a fluid flow using Terzaghi's law of effective stress [23]. Since the authors couple a Stokes and a Darcy flow outside and inside the porous medium, respectively, they have to stabilize the interface velocity and the Stokes flow with two non-physical parameters. A coupled FE approach for WCM that takes into account fluid–solid interaction was proposed by Poppe et al. [24]. Furthermore, some recent works focus on the extension of the description of fiber reinforcement deformations with anisotropic material behavior. Blais et al. [25] present a monolithic coupled FE approach to account for the porous deformations. They use an orthotropic FVF dependent approach for both the permeability and the stiffness of the porous medium, but assume that the transverse Poisson's ratio is zero and thus decouple transverse and in-plane stresses. Sarojini Narayana et al. [26] use an FE approach, in which the reinforcement behavior is represented as an orthotropic homogeneous medium, based on the approach of Celle et al. [9]. However, they only consider fibrous movements in the thickness direction, as their main focus is on the curing behavior of the infused resin.

Although much of the work on modeling fiber deformation due to fluid injection has been done using the FEM, a finite volume (FV) approach is used in this work because it has the advantage of automatically satisfying mass conservation and modeling air entrapment in a multiphase flow. Magagnato et al. [27] compare experimental results of the flow front around an integrated insert to the predictions of an FE tool and a multiphase FV approach. They show that the formation and especially the collapse of air inclusions can be predicted more accurately by the multiphase FV approach.

Some approaches for modeling deformations in an FV framework have already been investigated. Carrillo and Bourg [28] developed an FV open source solver, `hybridBiotInterFoam`, to model multiphase flow through a deformable porous solid in geomechanics. However, the model is only valid for small deformations and requires special constitutive equations to describe the interaction between multiphase flow and poro-mechanics. An FV approach to model orthotropic solid mechanics was presented by Demirdžić et al. [29], which was adopted by Cardiff [30] for muscles and a hip joint. The FV solid mechanics approach was extended for porous media by Tang et al. [31] and for large strains by Seuffert [14]. Both assume isotropic behavior for the porous medium.

However, for fiber reinforcements, the assumption of isotropic behavior leads to an overestimation of preform deformations and fiber
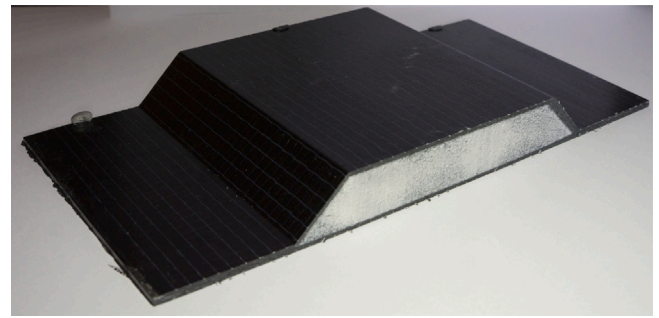

Fig. 1. Cross section of a Sandwich, manufactured intrinsically in CRTM, presented by Seuffert [14]. Deformations of the fiber reinforcement during infiltration not only occur in thickness direction but also in-plane, especially at the sidewalls and corners of the PET foam core.

displacements in the fiber direction. Typically, the compaction stiffness of the fabric is measured in the thickness direction and then used to describe the deformation behavior in all directions, while the flow velocities are highest in the fiber direction, which means that the error adds up. The errors are small as long as the deformations occur mainly in the thickness direction. This is no longer the case with complex geometries and with high local infiltration pressure gradients, for example near the inlet or around inserts. Another example is the manufacturing of a sandwich component with an integrated foam core in CRTM, as shown in Fig. 1 [14]. Due to the geometry and the deformations of the foam core, the fiber reinforcement is not only compacted in thickness direction but in-plane deformations can also occur during infiltration. The anisotropic fabric behavior is particularly relevant at the corners of the foam core and on the side walls.

Therefore, a three-dimensional, fully coupled FV approach of porous solid mechanics is proposed in this work, which captures the anisotropic stiffness of the fibrous structure. The approach is implemented in the RTM extension `OF-RTM-6` [32] of the Finite Volume toolbox `OpenFOAM` [33]. In particular, a method is presented to handle the stiffness tensor of fourth order in the `OpenFOAM` framework. Therefore, a decomposition into isotropic and anisotropic part is proposed and a method is presented to rotate the anisotropic stiffness tensor depending on local fiber orientations and to adapt it to the local fiber volume content. The fluid flow is described with a multiphase VOF approach that uses a unified mathematical description to account for porous zones and flow channels. The coupling between the porous deformations of the fiber reinforcement and the advancing resin is treated with an internal coupling to avoid volumetric mapping throughout the domain. An updated Lagrangian approach is used for the mesh motion. This method enables the prediction and analyzation of anisotropic deformations of fiber reinforcements during infiltration in the context of real applications.

2. Methodology

2.1. Fluid flow in porous media

The fluid injection is modeled with a multiphase approach accounting for the air phase in the unfilled regions. For interface tracking between resin and air, the Volume of Fluid (VOF) method is used, developed by Hirt and Nichols [34], allowing to obtain the velocity field by the mass continuity equation

$$\frac{\partial \rho}{\partial t} + \nabla \cdot (\rho \mathbf{u}) = 0, \tag{1}$$

with fluid density ρ and velocity $\mathbf{u}$, and the conservation form of the momentum continuity equation for a compressible Newtonian Fluid

$$\frac{\partial(\rho \mathbf{u})}{\partial t} + \nabla \cdot (\rho \mathbf{u} \otimes \mathbf{u}) = -\nabla p + \nabla \cdot (2\mu \mathbf{D}) - \frac{2}{3}\mu \nabla \mathrm{tr}(\nabla \mathbf{u}), \tag{2}$$

where $\otimes$ is the outer product, $\mathbf{D} = \mathrm{sym}(\nabla \mathbf{u})$ the rate of deformation tensor, p the pressure, and μ the dynamic viscosity. The fluid properties ρ and μ are determined by volume-weighted averaging $\rho = \alpha \rho_{\text{resin}} + (1 - \alpha) \rho_{\text{air}}$, where α is the volume share of resin in each cell.

To account for fluid flow through porous media and resin channels at the same time, a source term

$$\mathbf{Q}_{\text{Darcy}} = \nabla p_{\text{Darcy}} = -\mu \mathbf{K}^{-1} \tilde{\mathbf{u}} - \frac{1}{2} \rho \|\tilde{\mathbf{u}}\| F \tilde{\mathbf{u}}, \tag{3}$$

is added to the linear momentum equation, where $\tilde{\mathbf{u}} = (1 - \varphi)\mathbf{u}$ is the volume averaged velocity, with Fiber Volume Fraction (FVF) φ, permeability tensor $\mathbf{K}$, and inertial resistance coefficient F [35]. The right Darcy–Forchheimer term was rigorously derived for high Reynolds numbers by Whitaker [36]. However, for low Reynolds numbers $Re \ll 1$ the Forchheimer correction can be neglected in comparison to the viscous forces, leading to:

$$\frac{\partial(\rho \tilde{\mathbf{u}})}{\partial t} + \nabla \cdot (\rho \tilde{\mathbf{u}} \otimes \tilde{\mathbf{u}}) = -\nabla p + \nabla \cdot (\mu \nabla \mathbf{u}) + \nabla \cdot (\mu (\nabla \mathbf{u})^{\mathrm{T}}) \\ - \frac{2}{3} \mu \nabla (\nabla \cdot \mathbf{u}) - \mu \mathbf{K}^{-1} \tilde{\mathbf{u}}, \tag{4}$$

also used by Yang et al. [20] in a VOF approach in ANSYS Fluent.

For an incompressible fluid and low Reynolds numbers $Re \ll 1$, the inertia forces can also be neglected in comparison to the viscous forces. If additionally the permeability of the fiber semi-finished product is low, the porous drag dominates the flow behavior and Eq. (4) simplifies to Darcy's Equation [37] for stationary problems

$$\tilde{\mathbf{u}} = -\frac{\mathbf{K}}{\mu} \cdot (\nabla p) \tag{5}$$

inside the porous medium, which can also be derived directly from the Navier–Stokes-Equation as shown by Whitaker [38]. Outside the porous medium, the permeability is high and thus, the porous drag term vanishes and Eq. (2) is valid.

For moving cavities a mixed Lagrangian-Eulerian form is used, as proposed by Ferziger and Perić [39] and Jasak [40]. It is to be noted, that the mesh movement imposes an additional velocity $\mathbf{u}_s$. Thus, the fluid flux has to be corrected before solving the fluid linear momentum equation by $\mathbf{u} = \mathbf{u}_{\text{total}} - \mathbf{u}_s$. Otherwise the pressure would be influenced by the moving mesh velocity.

The permeability is modeled in a local cartesian coordinate system x' y' z' that is designed to be in the principal axis system of the fiber reinforcement. Thus, only the diagonal of the permeability tensor is occupied in the local coordinate system:

$$\mathbf{K}' = \begin{bmatrix} K_{11} & 0 & 0 \\ 0 & K_{22} & 0 \\ 0 & 0 & K_{33} \end{bmatrix} \mathbf{e}'_i \otimes \mathbf{e}'_j. \tag{6}$$

With this approach, global permeabilities can be defined based on experimental data. The local flow resistance is then derived in each cell, by interpolating the FVF-dependent permeability tensor to the local FVF and rotating it from the local fiber orientation to the global coordinate system.

2.2. Porous solid mechanics with updated Lagrangian formulation in FVM

The description of solid mechanics is usually based on the Lagrangian formulation and the weak form of the momentum conservation equation, using the Finite Element Method (FEM) for a numerical description. However, a cell-centered Finite Volume (FV) approach offers advantages for large deformations and for coupling of fluid and solid in a monolithic approach. First efforts to derive an FV method for solid mechanics were done by Demirdžić and Perić [41]. A summary of subsequent works is given by Cardiff and Demirdžić [42]. Cardiff and Tuković [43] implemented FV solid mechanics methods as `solids4foam` into the open-source framework `OpenFOAM`, extending the methods for large rotations and contact boundaries [30, 44], and for large strains and orthotropic material orientations [45].

Another extension was developed by Tang et al. [31], using the FV method for small-strain poro-elasticity. Seuffert [14] extended the FV poro-elasticity method for large deformations of isotropic materials.

This work builds on the previous developments to derive a solid mechanics FV poro-elasticity method for general anisotropic materials and locally varying material orientations. Based on the poro-elasticity extension of the updated Lagrangian formulation for small incremental strains by Tang et al. [31] a non-linear incremental formulation is developed to allow larger incremental deformations. The conservation of linear momentum for a general control volume Ω with surface Γ and unit normal $\mathbf{n}$ is given in integral form as:

$$\frac{\partial}{\partial t} \int_{\Omega} \rho_s \mathbf{u}_s \, d\Omega = \oint_{\Gamma} \mathbf{n} \cdot \boldsymbol{\sigma} \, d\Gamma + \int_{\Omega} \rho_s \mathbf{b} \, d\Omega \tag{7}$$

with solid velocity vector $\mathbf{u}_s$, effective stress tensor $\boldsymbol{\sigma}$, body force $\mathbf{b}$, and solid density ρ_s. This integral form of the equation is a strong form of conservation. In the FEM, a weak form is used. In solid mechanics, the deformations are usually smaller than in fluid mechanics, thus, the location can be described in Lagrangian formulation and the convection term of the time derivative of the displacement vanishes. Thus, the solid velocity $\mathbf{u}_s$ can be written as $\mathbf{u}_s = \partial \mathbf{d} / \partial t$, where $\mathbf{d}$ is the displacement.

As finite deformations are taken into account, the second Piola–Kirchhoff stress tensor

$$\mathbf{S} = J \mathbf{F}^{-1} \cdot \boldsymbol{\sigma} \cdot \mathbf{F}^{-\mathrm{T}} \tag{8}$$

is used, where the deformation gradient $\mathbf{F}$ and the Jacobian determinant J are derived from the displacements through

$$\mathbf{F} = \mathbf{I} + \nabla \mathbf{d} \tag{9}$$

$$J = \det(\mathbf{F}). \tag{10}$$

To deal with large deformations, an updated incremental Lagrangian formulation is used, where at the end of each time step the new configuration is set as reference configuration for the next timestep. To compute the updated Lagrangian form of the conservation of linear momentum, the updated form of the area element $d\Gamma_u$ has to be inserted, where the subscript u denotes the updated state. The current, deformed area element $d\Gamma$ can be derived from the reference area element by Nanson's equation $d\Gamma = J \mathbf{F}^{-\mathrm{T}} \cdot d\Gamma_u$ [46,47], where $d\Gamma_u$ is the area element of the last increment or the updated configuration in case of the updated Lagrangian approach.

Using the updated area element and replacing the Cauchy stress tensor by the second Piola–Kirchhoff stress tensor $\boldsymbol{\sigma} = J^{-1} \mathbf{F} \cdot \mathbf{S} \cdot \mathbf{F}^{\mathrm{T}}$, the momentum conservation Eq. (7) can be rewritten in an updated form, allowing for large deformations, as

$$\frac{\partial}{\partial t} \int_{\Omega} \rho_s \mathbf{u}_s \, d\Omega = \oint_{\Gamma_u} (\mathbf{F} \cdot \mathbf{S}) \, d\Gamma_u + \int_{\Omega_u} \rho_s \mathbf{b} \, d\Omega_u \\ = \oint_{\Gamma_u} \mathbf{n}_u \cdot (\mathbf{S} \cdot \mathbf{F}) \, d\Gamma_u + \int_{\Omega_u} \rho_s \mathbf{b} \, d\Omega_u. \tag{11}$$

Substituting the solid velocity by the derivative of displacement and using Terzaghi's law of effective stress [23] in terms of the second Piola Kirchhoff stress tensor

$$\mathbf{S}_{\text{total}} = \mathbf{S}_{\text{eff}} + \mathbf{S}_{\text{fluid}} \\ = \mathbf{S}_{\text{eff}} - p\mathbf{I} \tag{12}$$

Eq. (11) yields

$$\frac{\partial}{\partial t} \int_{\Omega} \rho_s \frac{\partial \mathbf{d}}{\partial t} \, d\Omega = \oint_{\Gamma_u} \mathbf{n}_u \cdot ((\mathbf{S}_{\text{eff}} - p\mathbf{I}) \cdot \mathbf{F}) \, d\Gamma_u + \int_{\Omega_u} \rho_s \mathbf{b} \, d\Omega_u. \tag{13}$$

As finite strains are taken into account, the strain is formulated by means of the Green–Lagrange strain tensor

$$\mathbf{E} = \frac{1}{2} \left(\nabla \mathbf{d} + \nabla \mathbf{d}^{\mathrm{T}} + \nabla \mathbf{d} \cdot \nabla \mathbf{d}^{\mathrm{T}} \right). \tag{14}$$

As an updated incremental Lagrangian approach is used to deal with large deformations, the strain increment is needed:

$$\delta \mathbf{E} = \frac{1}{2} \left(\nabla \delta \mathbf{d} + \nabla \delta \mathbf{d}^{\mathrm{T}} + \nabla \delta \mathbf{d} \cdot \nabla \mathbf{d}^{\mathrm{T}} + \nabla \mathbf{d} \cdot \nabla \delta \mathbf{d}^{\mathrm{T}} + \nabla \delta \mathbf{d} \cdot \nabla \delta \mathbf{d}^{\mathrm{T}} \right). \tag{15}$$

The idea of an updated approach is that the initial displacement in every time increment vanishes, following that

$$\delta \mathbf{E}_{\mathrm{u}} = \frac{1}{2} \left(\nabla \delta \mathbf{d} + \nabla \delta \mathbf{d}^{\mathrm{T}} + \nabla \delta \mathbf{d} \cdot \nabla \delta \mathbf{d}^{\mathrm{T}} \right), \tag{16}$$

$$\mathbf{F}_{\mathrm{u}} = \mathbf{I}. \tag{17}$$

To connect stress and strain, the St. Venant-Kirchhoff hyper-elastic constitutive relation

$$\mathbf{S}_{\mathrm{eff}} = \mathbb{C} : \mathbf{E}, \tag{18}$$

with the effective second Piola–Kirchhoff stress tensor $\mathbf{S}_{\mathrm{eff}}$, and the stiffness tensor $\mathbb{C}$, is used.

To compute the total Lagrangian results from the updated Lagrangian approach, the stress and strain rates have to be corrected to the current configuration with

$$\dot{\mathbf{E}} = \mathbf{F}^{\mathrm{T}} \cdot \dot{\mathbf{E}}_{\mathrm{u}} \cdot \mathbf{F}, \tag{19}$$

$$\dot{\mathbf{S}}_{\mathrm{eff}} = J \mathbf{F}^{-1} \cdot \dot{\mathbf{S}}_{\mathrm{eff,u}} \cdot \mathbf{F}^{-\mathrm{T}}. \tag{20}$$

However, with this correction the initial configuration has to be stored and referenced in each increment nevertheless. For problems with finite rotations and displacements, but small strains,

$$\dot{\mathbf{S}}_{\mathrm{eff,u}} = \mathbb{C} : \dot{\mathbf{E}}_{\mathrm{u}} \tag{21}$$

can be assumed.

Since the thickness direction is usually small in LCM processes, gravity and thus body forces can be neglected in good approximation. With this assumption and differentiation of Eq. (13), the incremental form

$$\frac{\partial}{\partial t} \int_{\Omega} \rho_{\mathrm{s,u}} \frac{\partial(\delta \mathbf{d})}{\partial t} \, \mathrm{d}\Omega = \oint_{\Gamma_{\mathrm{u}}} \mathbf{n}_{\mathrm{u}} \cdot \delta \mathbf{S}_{\mathrm{eff}} \, \mathrm{d}\Gamma_{\mathrm{u}}$$
$$- \oint_{\Gamma_{\mathrm{u}}} \mathbf{n}_{\mathrm{u}} \cdot \delta p \mathbf{I} \, \mathrm{d}\Gamma_{\mathrm{u}}$$
$$+ \oint_{\Gamma_{\mathrm{u}}} \mathbf{n}_{\mathrm{u}} \cdot \left[(\mathbf{S}_{\mathrm{eff}} - p\mathbf{I} + \delta \mathbf{S}_{\mathrm{eff}} - \delta p \mathbf{I}) \cdot \delta \mathbf{F} \right] \mathrm{d}\Gamma_{\mathrm{u}} \tag{22}$$

is derived, where the simplification of the updated form $\nabla \mathbf{d} = \mathbf{0}$ is used. Inserting the St. Venant Kirchhoff constitutive law from Eq. (18) and simplifying $\delta \mathbf{F} = \nabla \delta \mathbf{d}$ yields to

$$\frac{\partial}{\partial t} \int_{\Omega} \rho_{\mathrm{s,u}} \frac{\partial(\delta \mathbf{d})}{\partial t} \, \mathrm{d}\Omega = \oint_{\Gamma_{\mathrm{u}}} \mathbf{n}_{\mathrm{u}} \cdot \mathbb{C} : \delta \mathbf{E} \, \mathrm{d}\Gamma_{\mathrm{u}} - \oint_{\Gamma_{\mathrm{u}}} \mathbf{n}_{\mathrm{u}} \cdot \delta p \mathbf{I} \, \mathrm{d}\Gamma_{\mathrm{u}}$$
$$+ \oint_{\Gamma_{\mathrm{u}}} \mathbf{n}_{\mathrm{u}} \cdot \left[(\mathbf{S}_{\mathrm{eff}} - p\mathbf{I} + \delta \mathbf{S}_{\mathrm{eff}} - \delta p \mathbf{I}) \cdot \nabla \delta \mathbf{d} \right] \mathrm{d}\Gamma_{\mathrm{u}}. \tag{23}$$

Because of the calculation with Terzaghi's law of effective stress, there is an additional dependency on the fluid pressure in Eq. (23), allowing for a strong coupling between fluid flow and deformation of the porous domain.

The equations are solved with a staggered implicit–explicit algorithm. The second and third term on the right-hand side are rearranged as one source term and solved in a deferred correction approach. In this approach it is iterated over the source term in each timestep. The rest of the equation is solved implicitly.

The FVF and fiber orientation of the fiber preform are updated in every increment with

$$\varphi_{\mathrm{u}} = \delta J^{-1} \varphi, \tag{24}$$

$$\boldsymbol{\omega}_{\mathrm{u}} = \delta \mathbf{F}^{-1} \cdot \boldsymbol{\omega} \cdot \delta \mathbf{F}^{-\mathrm{T}}, \tag{25}$$

as the FVF has a huge influence on permeability and compaction behavior and thus, on the overall fluid flow.

2.3. A formulation for anisotropic solid deformation in FVM

For a hyper-elastic material the stiffness tensor has the main symmetry additionally to the left and right sub-symmetry and thus, the stress–strain-relation can be noted in Mandel Notation. In `OpenFOAM`,

tensors of fourth order are not implemented and cannot be solved internally. Thus, the stiffness tensor is split into four tensors of second order which can be handled separately, but depend on each other if the material is rotated. Analogously, the stresses and strains are divided into main components and mixed components, resulting in

$$\begin{bmatrix} S_{\mathrm{eff},11} \\ S_{\mathrm{eff},22} \\ S_{\mathrm{eff},33} \end{bmatrix} = \begin{bmatrix} C_{1111} & C_{1122} & C_{1133} \\ & C_{2222} & C_{2233} \\ \mathrm{sym.} & & C_{3333} \end{bmatrix} \begin{bmatrix} E_{11} \\ E_{22} \\ E_{33} \end{bmatrix}$$
$$+ \begin{bmatrix} \sqrt{2}C_{1123} & \sqrt{2}C_{1113} & \sqrt{2}C_{1112} \\ \sqrt{2}C_{2223} & \sqrt{2}C_{2213} & \sqrt{2}C_{2212} \\ \sqrt{2}C_{3323} & \sqrt{2}C_{3313} & \sqrt{2}C_{3312} \end{bmatrix} \begin{bmatrix} \sqrt{2}E_{23} \\ \sqrt{2}E_{13} \\ \sqrt{2}E_{12} \end{bmatrix}, \tag{26}$$

$$\begin{bmatrix} \sqrt{2}S_{\mathrm{eff},23} \\ \sqrt{2}S_{\mathrm{eff},13} \\ \sqrt{2}S_{\mathrm{eff},12} \end{bmatrix} = \begin{bmatrix} \sqrt{2}C_{1123} & \sqrt{2}C_{1113} & \sqrt{2}C_{1112} \\ \sqrt{2}C_{2223} & \sqrt{2}C_{2213} & \sqrt{2}C_{2212} \\ \sqrt{2}C_{3323} & \sqrt{2}C_{3313} & \sqrt{2}C_{3312} \end{bmatrix}^{\mathrm{T}} \begin{bmatrix} E_{11} \\ E_{22} \\ E_{33} \end{bmatrix}$$
$$+ \begin{bmatrix} 2C_{2323} & 2C_{2313} & 2C_{2312} \\ & 2C_{1313} & 2C_{1312} \\ \mathrm{sym.} & & 2C_{1212} \end{bmatrix} \begin{bmatrix} \sqrt{2}E_{23} \\ \sqrt{2}E_{13} \\ \sqrt{2}E_{12} \end{bmatrix}. \tag{27}$$

To improve the solution stability, the stiffness tensor is divided into an isotropic part and an anisotropic part by means of the Eigenprojectors as described by Bertóti and Böhlke [48]:

$$\mathbb{T}^{\mathrm{iso}} = (\mathbb{T} \cdot \mathbb{P}_1) \, \mathbb{P}_1 + \frac{1}{5} (\mathbb{T} \cdot \mathbb{P}_2) \, \mathbb{P}_2, \tag{28}$$

$$\mathbb{T}^{\mathrm{aniso}} = \mathbb{T} - \mathbb{T}^{\mathrm{iso}}, \tag{29}$$

where $\mathbb{P}_i$ are Eigenprojectors. The Projector representation of a general tensor is $\mathbb{T} = \sum_{\alpha=1}^{\gamma} \lambda_\alpha \mathbb{P}_\alpha$ with λ_α Eigenvalues.

The isotropic contribution to the stress divergence can be included in the implicit solution scheme by means of the Lamé parameters $\lambda_{\mathrm{L}}^{\mathrm{iso}} = K^{\mathrm{iso}} - \frac{2}{3} G^{\mathrm{iso}}$ and $\mu_{\mathrm{L}}^{\mathrm{iso}} = G^{\mathrm{iso}}$, which provide a scalar relation between stress and strain. $3K^{\mathrm{iso}}$ and $2G^{\mathrm{iso}}$ are the Eigenvalues of the isotropic part of the stiffness tensor, calculated from the Eigenprojectors as $K^{\mathrm{iso}} = \frac{1}{3}\mathbb{C} \cdot \mathbb{P}_1$ and $G^{\mathrm{iso}} = \frac{1}{10}\mathbb{C} \cdot \mathbb{P}_2$. The stress contribution by the anisotropic part of the stiffness tensor is added as explicit source term to the linear momentum equation. Therefore, the effective stress increment in the momentum conservation Eq. (23) is divided as follows:

$$\frac{\partial}{\partial t} \int_{\Omega} \rho_{\mathrm{s,u}} \frac{\partial(\delta \mathbf{d})}{\partial t} \, \mathrm{d}\Omega = \frac{1}{2} \oint_{\Gamma_{\mathrm{u}}} \mathbf{n}_{\mathrm{u}} \cdot \underbrace{(2\mu_{\mathrm{L}}^{\mathrm{iso}} + \lambda_{\mathrm{L}}^{\mathrm{iso}}) \nabla \delta \mathbf{d}}_{\delta \mathbf{S}_{\mathrm{eff}}^{\mathrm{iso}}} \mathrm{d}\Gamma_{\mathrm{u}}$$
$$+ \oint_{\Gamma_{\mathrm{u}}} \mathbf{n}_{\mathrm{u}} \cdot \underbrace{\left(\frac{1}{2}\mathbb{C} : (\nabla \delta \mathbf{d} + \nabla \delta \mathbf{d}^{\mathrm{T}} + \nabla \delta \mathbf{d} \cdot \nabla \delta \mathbf{d}^{\mathrm{T}}) - \frac{1}{2}(2\mu_{\mathrm{L}}^{\mathrm{iso}} + \lambda_{\mathrm{L}}^{\mathrm{iso}}) \nabla \delta \mathbf{d} \right)}_{\delta \mathbf{S}_{\mathrm{eff}}^{\mathrm{aniso}}} \mathrm{d}\Gamma_{\mathrm{u}}$$
$$- \oint_{\Gamma_{\mathrm{u}}} \mathbf{n}_{\mathrm{u}} \cdot \delta p \mathbf{I} \, \mathrm{d}\Gamma_{\mathrm{u}} + \oint_{\Gamma_{\mathrm{u}}} \mathbf{n}_{\mathrm{u}} \cdot \left[(\mathbf{S}_{\mathrm{eff}} - p\mathbf{I} + \delta \mathbf{S}_{\mathrm{eff}} - \delta p \mathbf{I}) \cdot \delta \mathbf{F} \right] \mathrm{d}\Gamma_{\mathrm{u}} \tag{30}$$
$$= \frac{1}{2} \oint_{\Gamma_{\mathrm{u}}} \mathbf{n}_{\mathrm{u}} \cdot (2\mu_{\mathrm{L}}^{\mathrm{iso}} + \lambda_{\mathrm{L}}^{\mathrm{iso}}) \nabla \delta \mathbf{d} \, \mathrm{d}\Gamma_{\mathrm{u}} + \oint_{\Gamma_{\mathrm{u}}} \mathbf{n}_{\mathrm{u}} \cdot \mathbf{Q}_{\mathrm{explicit}} \, \mathrm{d}\Gamma_{\mathrm{u}},$$

where $\mathbf{Q}$ is calculated as explicit source term in each increment.

The anisotropic part of the stiffness tensor is rotated in each cell from the local material orientation to the global coordinate system in each increment. Like this, it is accounted for fiber-reorientation due to reinforcement deformations. Furthermore, one orthotropic stiffness can be defined globally in a main axis system, which is adapted to the local orientation state and FVF in each cell. The local stiffness tensors are rotated by means of the rotation tensor of fourth order $\mathbb{R} = \mathbf{R} \,\square\, \mathbf{R}^{\mathrm{T}}$, where $\square$ is the box product defined as $(A \,\square\, B)_{ijkl} = A_{ik} B_{lj}$ in index notation, to the global orientation, so

$$\mathbb{C}_{\mathrm{global}} = \mathbb{R}^{\mathrm{T_M}} \mathbb{C}_{\mathrm{local}} \mathbb{R}. \tag{31}$$

$\mathbb{A}^{\mathrm{T_M}}$ is the major transpose of a tensor of 4th order meaning $A_{ijkl}^{\mathrm{T_M}} = A_{klij}$. The isotropic part is calculated from the unrotated stiffness tensor to safe computational cost as the isotropic constants are independent of the material orientation.

As the stiffness tensor is separated in four tensors of second order, the rotation has to be performed in Mandel notation, which was shown to be valid for fourth order tensors with left and right sub-symmetry by Koay [49] and Mehrabadi et al. [50] as the non symmetric part of the rotation tensor is filtered by the stiffness tensor. In Mandel Notation the fourth-order Rotation tensor can be derived from the second-order rotation tensor

$$\mathbf{R} = \begin{bmatrix} R_{11} & R_{12} & R_{13} \\ R_{21} & R_{22} & R_{23} \\ R_{31} & R_{32} & R_{33} \end{bmatrix} \tag{32}$$

to be

$$\mathbb{R} = \begin{bmatrix} \mathbf{R}_{[1]} & \mathbf{R}_{[2]} \\ \mathbf{R}_{[3]} & \mathbf{R}_{[4]} \end{bmatrix} \tag{33}$$

with the components

$$\mathbf{R}_{[1]} = \begin{bmatrix} R_{11}^2 & R_{12}^2 & R_{13}^2 \\ R_{21}^2 & R_{22}^2 & R_{23}^2 \\ R_{31}^2 & R_{32}^2 & R_{33}^2 \end{bmatrix}, \tag{34}$$

$$\mathbf{R}_{[2]} = \begin{bmatrix} \sqrt{2}R_{12}R_{13} & \sqrt{2}R_{11}R_{13} & \sqrt{2}R_{11}R_{11} \\ \sqrt{2}R_{22}R_{23} & \sqrt{2}R_{21}R_{23} & \sqrt{2}R_{21}R_{22} \\ \sqrt{2}R_{32}R_{33} & \sqrt{2}R_{31}R_{33} & \sqrt{2}R_{31}R_{32} \end{bmatrix}, \tag{35}$$

$$\mathbf{R}_{[3]} = \begin{bmatrix} \sqrt{2}R_{21}R_{31} & \sqrt{2}R_{22}R_{33} & \sqrt{2}R_{23}R_{33} \\ \sqrt{2}R_{11}R_{31} & \sqrt{2}R_{12}R_{32} & \sqrt{2}R_{13}R_{33} \\ \sqrt{2}R_{11}R_{21} & \sqrt{2}R_{12}R_{22} & \sqrt{2}R_{13}R_{23} \end{bmatrix}, \tag{36}$$

and

$$\mathbf{R}_{[4]} = \begin{bmatrix} R_{22}R_{33} + R_{23}R_{32} & R_{21}R_{33} + R_{23}R_{31} & R_{21}R_{32} + R_{22}R_{31} \\ R_{12}R_{33} + R_{13}R_{32} & R_{11}R_{33} + R_{13}R_{31} & R_{11}R_{32} + R_{12}R_{31} \\ R_{12}R_{23} + R_{13}R_{22} & R_{11}R_{23} + R_{13}R_{21} & R_{11}R_{22} + R_{12}R_{21} \end{bmatrix}. \tag{37}$$

The rotated stiffness parts are used to calculate the momentum balance and to update the total stress in the last iteration.

As fabrics show highly nonlinear compaction behavior depending on FVF, a hyperelastic approach is implemented. It is assumed that the dependency on fiber content is equal in all material directions, because the main deformations occur in thickness direction and deformations are rather small in fiber direction. Thus, initial values are set for each stiffness component and scaled thereafter piecewise linearly by FVF:

$$E_{\text{hyper}}(\varphi) = \begin{cases} E_0 + (E_1 - E_0)\varphi, & \forall \varphi \in [\varphi_0, \varphi_1] \\ \dots \\ E_i + (E_{i+1} - E_i)\varphi, & \forall \varphi \in [\varphi_i, \varphi_{i+1}] \end{cases} \tag{38}$$

$$C_{jklm,\text{hyper}}(\varphi) = C_{jklm}^0 \frac{E_{\text{hyper}}(\varphi)}{E_0} \tag{39}$$

If the deformations are small, what can usually be assumed for an updated approach, the simulation approach can be changed to an infinitesimal strain approach to save computational cost. For small deformations Tang et al. [31] state that it can be assumed

$$d\mathbf{\Gamma} = d\mathbf{\Gamma}_{\text{u}} \tag{40}$$

for the surface increment and for the strain increment

$$\delta\boldsymbol{\varepsilon} = \frac{1}{2}\left(\nabla\delta\mathbf{d} + \nabla\delta\mathbf{d}^{\text{T}}\right) = \delta\boldsymbol{\varepsilon}_{\text{u}}. \tag{41}$$

The general form of the conservation equation of linear momentum for small deformations thus simplifies to

$$\frac{\partial}{\partial t} \int_{\Omega} \rho_{\text{s,u}} \frac{\partial(\delta\mathbf{d})}{\partial t} d\Omega = \frac{1}{2} \oint_{\Gamma_{\text{u}}} \mathbf{n}_{\text{u}} \cdot \mathbb{C} : (\nabla\delta\mathbf{d} + \nabla\delta\mathbf{d}^{\text{T}}) d\Gamma_{\text{u}} - \oint_{\Gamma_{\text{u}}} \mathbf{n}_{\text{u}} \cdot p\mathbf{I} d\Gamma_{\text{u}}, \tag{42}$$

while stiffness rotation and calculation stay the same.

2.4. Fluid structure interaction for fluid flow through porous media

The implementation of fluid flow and moving meshes is based on an OpenFOAM extension accounting for anisotropic porous drag, during and changing FVF with moving meshes by Bernath et al. [32]. Based on the FV approaches for modeling CRTM and pressure-controlled RTM (PC-RTM) by Seuffert et al. [35,51], the solution algorithm is extended with the anisotropic porous solid mechanics approach described in the previous sections. A monolithic approach is chosen to avoid time consuming volumetric coupling in the whole cavity. Therefore, in an iterative solution scheme first the poro-elasticity is solved, and stresses and strains are updated depending on the calculated incremental displacements. Secondly, the fluid flow is calculated depending on the stresses and displacements of the porous medium. This procedure is repeated until a common solution is found. The solution procedure is illustrated in Fig. 2.

For the porous mechanics calculation at first, the Lamé parameters are gained from the isotropic stiffness part to setup the implicit equation. If the stiffness is defined to be anisotropic, the local material orientations are derived from the fiber orientation and thickness direction and the local stiffness tensors are rotated from their main axis systems in the material coordinate system to the global orientation, where stress and strain increments are calculated. Either from the anisotropic incremental stresses or from the incremental strains and Lamé parameters and from the pressure, the explicit source term is calculated as described in Eq. (30) and Eq. (23), respectively.

Thereafter, the momentum conservation equation is solved for poromechanics and stress and strain increments are calculated. If the porous solid mechanics solution converges, the total values are updated with the incremental results and the mesh is moved accordingly. The mesh movement is governed by the solid mechanics equations. The fluid influences the mesh deformation only indirectly via the fluid pressure in the linear momentum equation. Before solving for the fluid flow, FVF and fiber orientation are updated to the deformed mesh according to Eqs. (24) and (25). If no convergence is reached, the total values have to be set back to the values of the last stable time step. The incremental displacements are relaxed using the values from the current and last increment and the loops are repeated until convergence is reached.

3. Verification

For fiber structures, the orthotropic material behavior is of special relevance and is therefore used for verification of the developed method. Non-orthotropic deformation behavior can also be prescribed, for example for sheared textiles, as long as the material coordinate system is described in an orthonormal system. In the orthotropic case, the number of independent material parameters reduces to nine and the entries of the stiffness tensor depending on engineering constants in the main axis system are:

$$\begin{aligned} C_{1111} &= \frac{1 - \nu_{23}\nu_{32}}{D} E_1, & C_{2222} &= \frac{1 - \nu_{13}\nu_{31}}{D} E_2, \\ C_{3333} &= \frac{1 - \nu_{12}\nu_{21}}{D} E_3, & C_{1122} &= \frac{\nu_{21} - \nu_{23}\nu_{31}}{D} E_1, \\ C_{1133} &= \frac{\nu_{31} - \nu_{32}\nu_{21}}{D} E_1, & C_{2233} &= \frac{\nu_{32} - \nu_{31}\nu_{12}}{D} E_2, \\ C_{2323} &= G_{23}, & C_{1313} &= G_{13}, \\ C_{1212} &= G_{12}, \end{aligned} \tag{43}$$

with $D = 1 - \nu_{12}\nu_{21} - \nu_{31}\nu_{13} - \nu_{32}\nu_{32} - 2\nu_{12}\nu_{23}\nu_{31}$.

The engineering constants are used as input parameters in the verification cases. Two separate verifications are introduced in the following: a unidirectional fluid-driven deformation according to MacMinn et al. [52] to account for the fluid–solid interaction in porous solid mechanics, and a two-dimensional hole in a plate test according to Cardiff et al. [45] to verify the anisotropic stiffness implementation against an analytical solution.
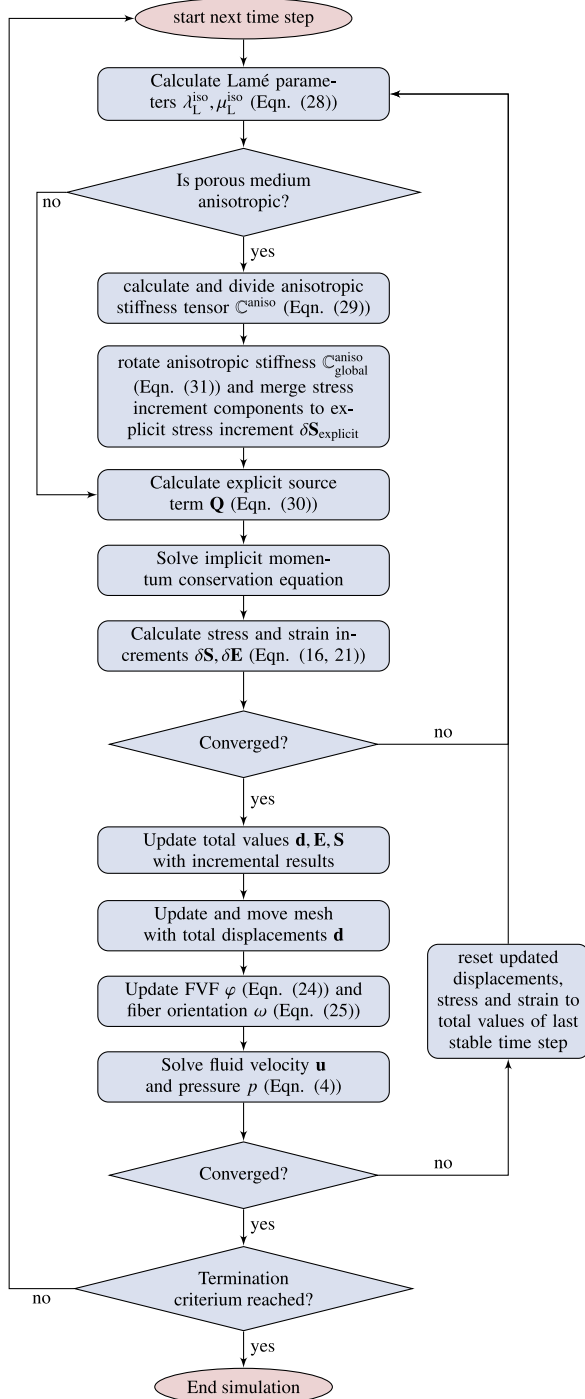
Fig. 2. Solution scheme accounting for the fluid–solid interaction of resin flow and porous fiber reinforcement, extended for anisotropic porous solid mechanics from Seuffert [14].
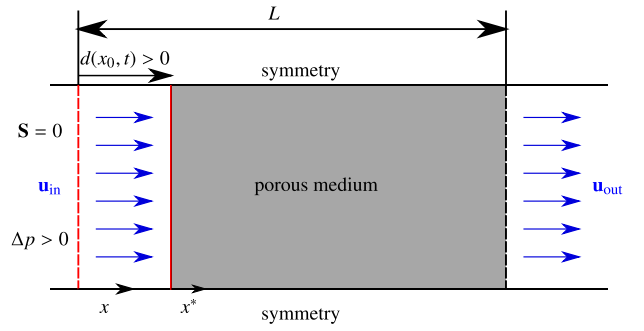

Fig. 3. Schematic representation of the verification case by MacMinn et al. [52] for a fluid-driven compression of a porous medium taking into account large strains [14]. The porous medium (light gray) with initial length L is fixed at the right boundary by a permeable wall, indicated by a dashed black line, and compressed by a fluid flow (blue arrows) in x-direction until a steady state is reached. The dashed red line indicates the initial position of the porous medium and the red line the porous boundary in compressed state. The displacement is described by $d(x, t)$. (For interpretation of the references to color in this figure legend, the reader is referred to the web version of this article.)

Table 1
Summary of process parameters and material data used for the fluid-driven verification case after MacMinn et al. [52].

Parameter	Value	Description
L	1 m	initial length of the porous medium
p_{inlet}	600 kPa	fluid pressure at inlet
p_{outlet}	100 kPa	fluid pressure at outlet
φ_0	0.5	initial FVF
λ_{L}	0	first Lamé constant
$\mu_{\text{L}}(\varphi = 0.5)$	0.5 MPa	(initial) second Lamé parameter
$\mu_{\text{L}}(\varphi = 1)$	5 MPa	second Lamé parameter at FVF of 100%
K_{11}^0	10^{-10} m^2	(initial) permeability
A_{Gebart}	2×10^{-10} m^2	Gebart model parameter

3.1. Uniaxial fluid driven deformation test case as proposed by MacMinn et al. [52]

In the following, the porous solid mechanics approach is verified against the results of MacMinn et al. [52] and Seuffert [14] for a uniaxial flow-induced deformation of a porous medium.

The fluid-driven compression test case is illustrated in Fig. 3. It is assumed that the lateral boundaries are rigid, frictionless and imperme-able. Thus, the case is independent of the shape and size of the cross section in y-z-direction. On the right hand side, the porous medium is fixed by a permeable wall and on the left side, fluid is injected with a constant pressure gradient, compressing the porous medium.

Four complexity levels are considered:

1. linear, constant permeability K and constant Lamé parameters μ_{L}, λ_{L}
2. geometric non-linear, constant permeability K and constant Lamé parameters μ_{L}, λ_{L}
3. geometric non-linear, non-constant permeability $K(\varphi)$ and constant Lamé parameters μ_{L}, λ_{L}
4. geometric non-linear, non-constant permeability $K(\varphi)$ and non-constant Lamé parameters
   $\mu_{\text{L}}(\varphi)$, $\lambda_{\text{L}}(\varphi)$

As a one-dimensional problem is investigated, the permeability tensor reduces to a scalar permeability K_{11} in fiber direction. For the non-constant permeability, a Gebart type permeability is used with $K_{11} = K_{\parallel} = A_{\text{Gebart}} \cdot \frac{(1-\varphi)^3}{\varphi^2}$, based on Gebart [53] with $A_{\text{Gebart}} = \frac{8r^2}{c}$. The variable c depends on the fiber distribution type, and r is the fiber radius. The non-constant Lamé parameters are formulated depending on the FVF with a hyperelastic approach, implementing a piecewise linear dependency between FVF and Lamé parameters, according to Eqs. (38) and (39). The process parameters and material data are summarized in Table 1.

A one-dimensional mesh is used with one element in y- and z-direction and 100 elements in x-direction. A mesh density study was performed (Appendix A), showing that the mesh converges for more than 40 elements in x-direction. To enhance convergence, the velocity is increased over 25 timesteps. Depending on the prescribed material
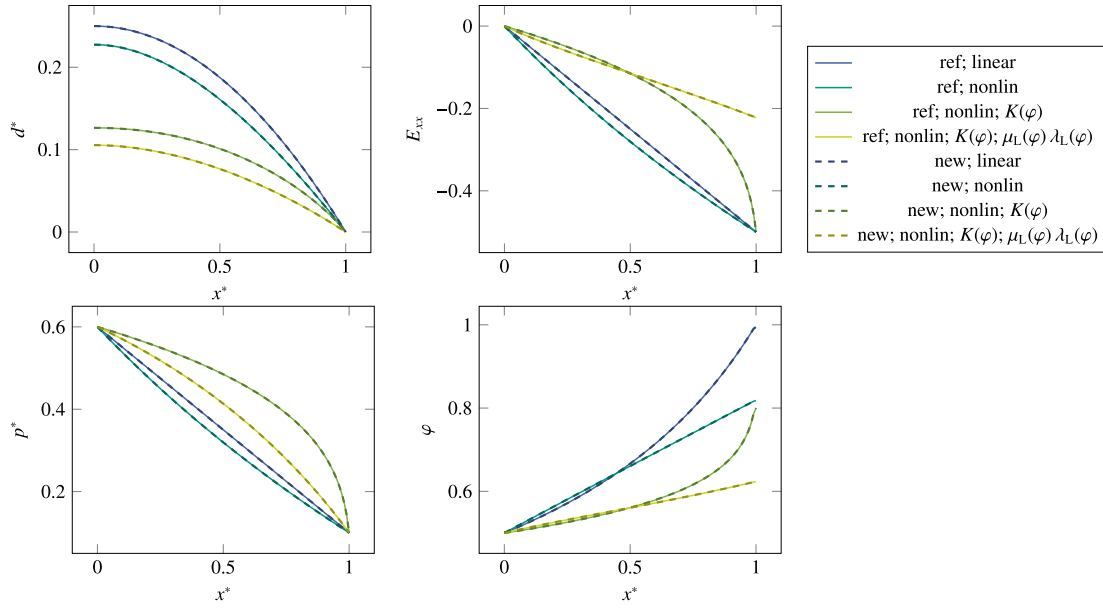
Fig. 4. Comparison of the four internal coupling verification cases along the normalized deformed state of the porous medium x^* to the reference results of Seuffert [14] (ref): Normalized displacement d^*, component E_{xx} of Green–Lagrange strain tensor, normalized pressure p^*, and FVF φ from top left to bottom right.

model, 7 to 13 outer iterations are necessary in each time step to reach convergence.

In Fig. 4, displacement, Green–Lagrange strain, pressure and FVF over the normalized length x^* of the deformed state are compared, for the four introduced simplifications. The comparison is carried out when a state of equilibrium is reached, in a normalized form with

$$x^* = \frac{x - d(x)}{L},$$
$$\mathbf{S}^* = \frac{\mathbf{S}}{E_{\varphi=0.5}},$$
$$d^* = \frac{d}{L}, \text{ and} \tag{44}$$
$$p^* = \frac{p}{E_{\varphi=0.5}}.$$

Exact agreement with the results of MacMinn et al. [52] and Seuffert et al. [54] can be observed. It is to be noted, that the purely linear model leads to a non-physical FVF of 1 at the porous wall. This model is not sufficient to describe the fiber semi-finished product deformations, which is why non-linear models with material behavior dependent on the FVF are considered in the following. The FVF-dependent permeability shows the largest influence on filling pressure and displacement, while the non-linearity of the process is rather decreased by an FVF-dependent fabric stiffness.

3.2. 2D Hole-in-a-plate orthotropic solid deformation test case as proposed by Cardiff [30]

To verify the anisotropic material definition and rotation, simulations with varying stiffness in transverse direction are performed on a two-dimensional plate with a hole in the middle as shown in Fig. 5, analogously to the verification case proposed by Cardiff [30]. For this case small deformations are assumed. For a two-dimensional open-hole tension test, an analytical solution for the hoop stress on the surface of the hole was derived by Lekhnitskii [55] depending on the rotation angle θ with

$$\sigma_{\theta\theta} = T \frac{-k \cos^2 \theta + (1 + n) \sin^2 \theta}{\sin^4 \theta + (n^2 - 2k) \sin^2 \theta \cos^2 \theta + k^2 \cos^4 \theta}, \tag{45}$$
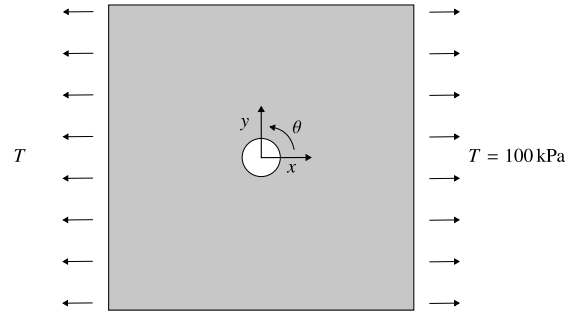

Fig. 5. Schematic representation of the two-dimensional open-hole-tension verification case for an orthotropic material under traction.

where T is the traction applied in x-direction and k and n are parameters derived from the material stiffness as

$$k = \sqrt{\frac{E_x}{E_y}}, \tag{46}$$

$$n = \sqrt{2k + \frac{E_x}{G_{xy}} - 2\nu_{xy}}, \tag{47}$$

respectively. The stresses in the global cartesian coordinate system can be derived from the hoop stress $\sigma_{\theta\theta}$ as follows:

$$\sigma_{xx} = \sigma_{\theta\theta} \sin^2 \theta, \tag{48}$$

$$\sigma_{yy} = \sigma_{\theta\theta} \cos^2 \theta, \tag{49}$$

$$\sigma_{xy} = -\sigma_{\theta\theta} \sin \theta \cos \theta. \tag{50}$$

The plate has a length of $L = 8$ m with a hole diameter of $d = 0.6$ m. It is loaded with a traction of $T = 100$ kPa in x-direction. Rigid body rotations and displacements of the plate are prevented by fixing the bottom left corner. The material behavior is defined with $E_x = 200$ GPa, $G_{xy} = 76.923$ GPa, $\nu_{xy} = 0.3$, and E_y varying between 60 GPa and 200 GPa. To eliminate finite domain size effects the analytical traction is prescribed at the boundaries as described by Demirdžić et al. [56].

The resulting analytical and numerical stresses for different degrees of anisotropy are depicted in Fig. 6. The numerical results show the
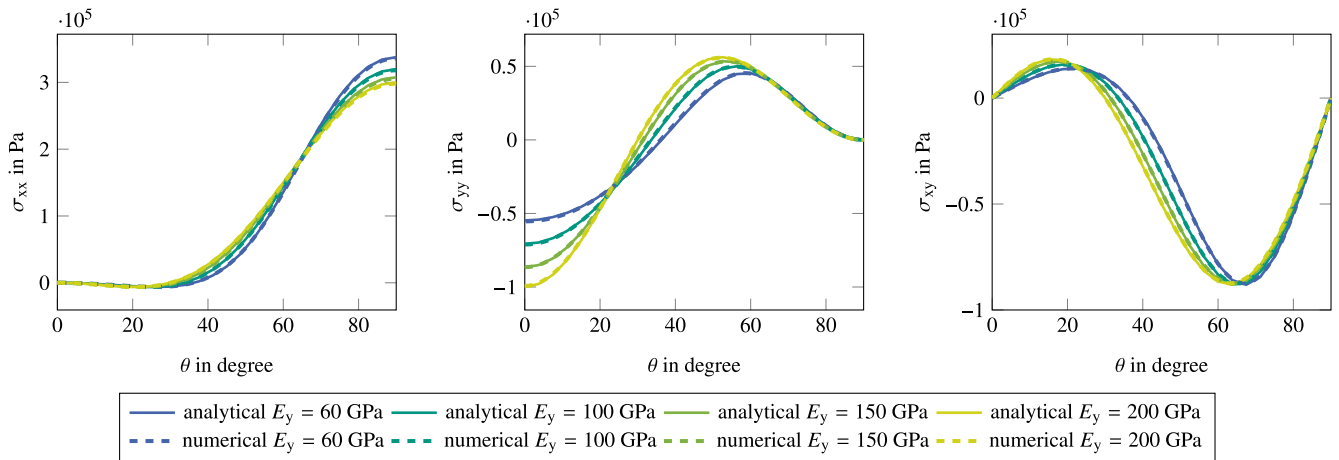
Fig. 6. Comparison of analytical and numerical normal stresses σ_{xx}, σ_{yy} and shear stress σ_{xy} around the hole depending on rotation angle θ based on Cardiff [30] and the analytical solution of Lekhnitskii [55].

same qualitative and quantitative behavior as the analytical solution, although slight differences occur due to the different assumptions made for the numerical and analytical solution. Different discretizations were investigated to ensure convergence of the numerical predictions towards the analytical solution (Appendix B, Fig. 12). Moreover, different dimensions of the cutout were analyzed to ensure from which size of the hole an infinitely extended domain can be assumed in comparison to the hole dimensions (Appendix B, Fig. 13). In accordance with these preliminary investigations, a mesh density of 960x960 elements and the above given diameter of 0.6 m were selected.

There are some differences between the assumptions of the analytical and numerical approach, which lead to small deviations in the stress calculation. An obvious difference to the analytical solution is the finite domain size, which is necessary for a numerical solution. This was addressed by adapting the traction boundary conditions accordingly and by examining different ratios between domain size and cutout radius (Appendix B, Fig. 13) to ensure that the assumption of a finite domain size can be justified. The clamping at the corner can also influence the resulting stresses, even if it is far from the hole circumference under consideration. However, the influence is assumed to be small, which was verified by comparison to a symmetric calculation of a quarter of the plate.

In addition, a plane stress state and a 2D problem are assumed for the analytical solution, which have to be introduced analogously in the simulation. For 2D formulations in the Finite Volume method, a thickness of the geometry in the neglected spatial direction is necessary to generate a volume through which 2D fluxes can be solved. The top and bottom boundary faces are fixed to keep the geometrical height constant and realize a 2D flow. Therefore, a plane strain state is introduced by the choice of displacement boundary conditions. To decouple the stress calculation from the third spatial direction the transverse contraction coefficients in this direction are chosen to be zero. Thus, a plane stress state can be achieved. Overall, the agreement between the numerical and analytical solution is considered to be quite accurate.

Different stress states arise for the investigated degrees of anisotropy. This can be observed mainly for the normal stress in y-direction but also for the shear stress progression along the hole. The absolute value of the normal stress σ_{yy} at the hole is almost double for the nearly isotropic case with $E_y = 200$ GPa compared to the results with highest anisotropy ($E_y = 60$ GPa). This difference shows the impact of the new adapted model on the stress response. The effect on the filling behavior of a plate in CRTM is analyzed in the following.
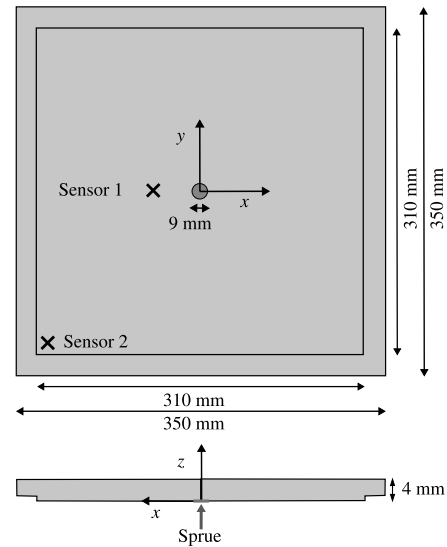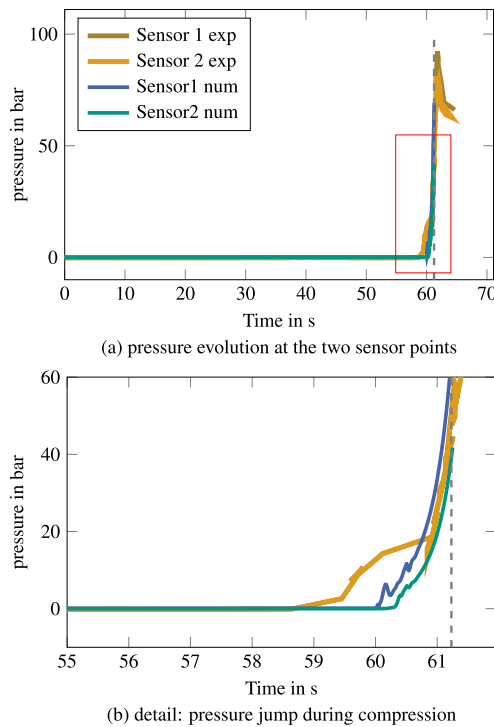

Fig. 7. Schematic representation of infiltration application example of a three-dimensional plate as presented by Sarojini Narayana et al. [57].

3.3. Experimental validation example: Isotropic and anisotropic poro-elasticity in a 3D flow under compaction

In order to validate the accuracy of the numerical model presented, the filling of a three-dimensional plate with a point sprue in the center and a fiber clamping at the edges is calculated. The material data and geometric data of Sarojini Narayana et al. [57] are used for this purpose. A schematic representation of the validation case is given in Fig. 7. Based on the flow front curves presented by Sarojini Narayana et al. [57] in partially filled states as well as the pressure curves at the two sensor points (Figure 13 in [57]), the numerical predictions of the newly developed model are validated against the experimental results.

The plate of length $L = 350$ mm and initial height $H = 4$ mm is infiltrated with constant velocity u_{in} through a 9 mm wide inlet in the middle of the lower mold as shown in Fig. 7. The lower wall ($z = 0$) is fixed, while the upper wall is moved with constant velocity $u_s = -1$ mm/s after an injection time of 60 s until the plate is compressed to its final height of 3 mm. The initial FVF is 42% in the domain and 51% in the fiber clamping, which is compressed to a final FVF of 56% and 72.7%, respectively. Sarojini Narayana et al. [57] assume a gap

(a) pressure evolution at the two sensor points

(b) detail: pressure jump during compression

Fig. 8. Validation of the numerically predicted pressure evolution over time at the two sensor points compared to the experimentally measured pressures by Sarojini Narayana et al. [57].
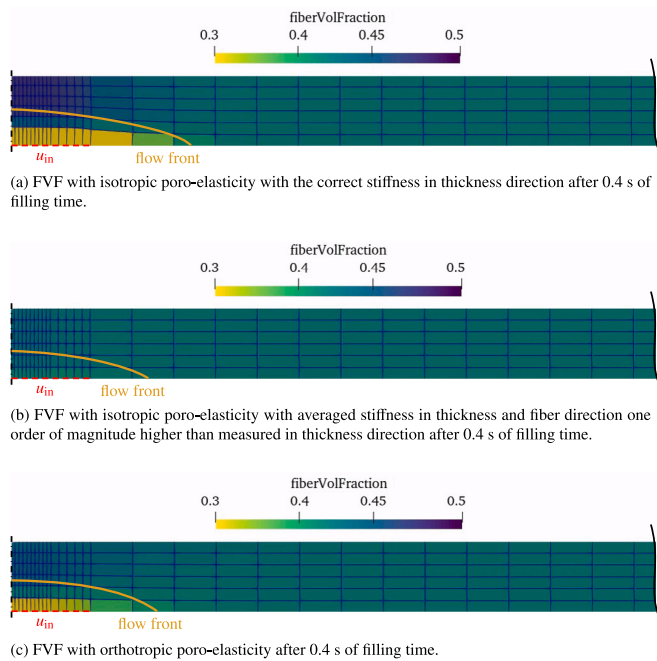

Fig. 9. Flow front evolution over time in the diagonal of the plate predicted by the presented model compared to the experimental and numerical results (ref) by Sarojini Narayana et al. [57].

between upper mold and fiber reinforcement for their displacement calculations. However, they calculate pressure and flow front evolution with an initially homogeneous FVF over the thickness of the cavity. Due to the relaxation behavior of the semi-finished fiber product and the relatively small gap, the semi-finished product is expected to expand in the thickness direction over the entire initial height of the cavity. Therefore, analogous to Sarojini Narayana et al. [57], a homogeneous FVF over the height is assumed as the initial state.

On the surrounding sides the porous medium is constrained by porous walls, where the fluid can flow out and the vent pressure is applied. The resin is injected at room temperature (20 °C) and the molds are heated to 100 °C (upper mold) and 95 °C (lower mold). The temperature and cure dependent viscosity of the resin is considered with a Castro Macosko model [58] analogous to Sarojini Narayana et al. [57] and the cure rate is modeled with an Arrhenius type equation. For the material parameters the reader is referred to Sarojini Narayana et al. [57].

In Fig. 8, the pressure at the two sensor points (highlighted in Fig. 7) over time is compared to the experimental results by Sarojini Narayana et al. [57]. The same qualitative behavior can be observed for the numerical predictions and the experimental results during infiltration and compression phase. During infiltration (up to 60 s) the pressure stays at a low level and then quickly rises when compression starts. It is to be noted that the simulation was stopped after 61.25 s when the mold reaches its final height. Therefore, the pressure drop observed in the experiments after compaction is not considered in the numerical results. The end of compression is marked by a dashed line. At this time the maximum pressure predicted by the numerical solution is 68 bar for the first Sensor, which fits to the final pressure of Sensor one in the experiments after the overshoot.

Moreover, in Fig. 9 the evolution of the flow front over time is compared with the numerical and experimental results by Sarojini Narayana et al. [57]. Since the pressure at the inlet is ramped up over the first five seconds to improve numerical stability, the flow front
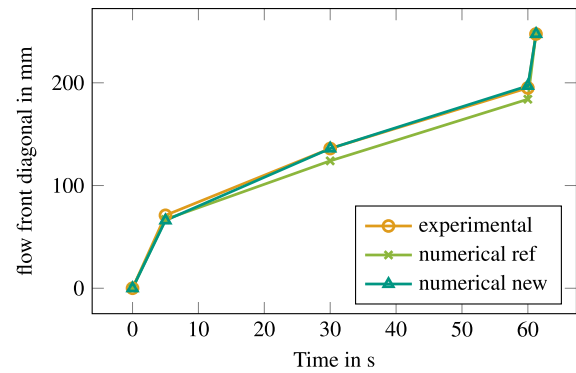
is slightly too slow in the beginning. Despite this start-up behavior, the filling can be predicted quite accurately and the prediction of the flow front is closer to the experimental measurements than with the numerical model of Sarojini Narayana et al. [57].

To illustrate the difference between the isotropic and the anisotropic stiffness model, the FVF near the inlet is shown in Fig. 10 for two different assumptions for the isotropic stiffness and one orthotropic case. Different mesh configurations have been analyzed to ensure mesh independence for the chosen configuration (Appendix C, Fig. 14). For the isotropic approach, one solution is shown with an isotropic stiffness equal to the stiffness measured by Sarojini Narayana et al. [57] in thickness direction (Fig. 10(a)). However, these simulations are not stable due to element deformations in in-plane direction. Therefore, it was necessary to average the reinforcement stiffness in the thickness direction and the in-plane directions to reduce element deformations in the fiber directions (Fig. 10(b)). This led to a stiffness, which is one order of magnitude higher than the stiffness measured by Sarojini Narayana et al. [57] and therefore an overestimation of the stiffness in thickness direction. For the anisotropic approach, an orthotropic material model was prescribed using the compaction stiffness measured by Sarojini Narayana et al. [57] in the thickness direction and specifying an in-plane stiffness which is two orders of magnitude higher. Sarojini Narayana et al. [57] calculated stresses and deformations only in the thickness direction of the plate and fixed the degrees of freedom for in-plane deformations.

It can be observed, that the high fluid pressure gradient at the inlet leads to a movement of fibers towards the upper mold for all considered stiffness models, which was also reported by Sarojini Narayana et al. [57]. In the isotropic simulation with low stiffness, elements are additionally dragged in the in-plane direction towards the outlet by the inlet pressure, leading to element deformations as well as a reduced FVF at the inlet (see Fig. 10(a)) compared to the orthotropic model (Fig. 10(c)). This can be explained by an overestimation of reinforcement elongation along fiber direction due to equal material stiffness in all directions. It is to be noted, that the simulation crashes shortly after the shown comparison due to element distortions. Although the presented approach is capable of handling flow through porous zones and pure resin flow, the formation of new pure fluid zones during infiltration cannot be captured. The fiber volume content reduces near the inlet due to fluid pressure but cannot reach zero because fibers are not transported over cell boundaries. Therefore, the approach is able to predict fiber deformations in a homogenized form only to a certain extend. If local deformations get too high, distorted elements can occur, which lead to a termination of the simulation. However, element deformations in fiber direction are decreased by the anisotropic approach compared to the isotropic one.

(a) FVF with isotropic poro-elasticity with the correct stiffness in thickness direction after 0.4 s of filling time.

(b) FVF with isotropic poro-elasticity with averaged stiffness in thickness and fiber direction one order of magnitude higher than measured in thickness direction after 0.4 s of filling time.

(c) FVF with orthotropic poro-elasticity after 0.4 s of filling time.

Fig. 10. Comparison of FVF distribution near the inlet in a three-dimensional plate with isotropic ((a) stiffness equals measured stiffness in thickness direction, but simulation is instable, and (b) averaged stiffness one order of magnitude higher than the measured stiffness in thickness direction) and (c) orthotropic poro-elastic behavior of the fabric. Due to the slender structure, the symmetry of the plate at the center line is used to better represent the behavior at the inlet and the plate is cut off towards the edge. The inlet is indicated in red and the flow front at the given time in orange. Depending on the stiffness model, the fiber reinforcement is deformed to varying degrees by the fluid pressure at the inlet, which is reflected in the change in the FVF. This in turn has a strong influence on the permeability and therefore the flow behavior.

The stable isotropic model with high stiffness (Fig. 10(b)) leads to an underestimation of deformations and the FVF changes from 42% to 40% at the inlet. As the stiffness of the real porous material is quite high in fiber direction, it would be expected that no fiber movements occur along x-direction, but a shift of fibers at the inlet towards the upper mold due to the pressure gradient in thickness direction at the inlet. That is, what can be observed for the orthotropic model (Fig. 10(c)), illustrating the use of the developed anisotropic porous solid mechanics model. Moreover, the simulation is more stable than the isotropic approach using the same stiffness in thickness direction. Due to the strong influence of the fiber volume content on the permeability, the flow front velocity also changes under pressure boundary conditions at the inlet depending on the stiffness of the fiber reinforcement.

4. Conclusion

In this work a general anisotropic and three-dimensional finite volume approach for porous solid mechanics was derived and verified with two different tests to adequately capture the fluid-solid interaction inside the porous medium as well as the anisotropic material behavior. This makes it possible to analyze and predict the anisotropic deformation behavior of fiber reinforcements during infiltration in the context of real applications. To describe the anisotropic behavior of the fiber reinforcement, a method was presented to decompose and rotate the stiffness tensor of 4th order to account for local fiber orientation and local fiber content. It was shown that the derived approach is suitable for modeling fluid flow induced deformations of the porous medium and the resulting stresses in the anisotropic reinforcement.

Furthermore, the pressure and flow front predictions of the proposed model have been validated against experimental and numerical

results from literature for the infiltration of a three-dimensional plate in CRTM. A good agreement between the results of the new model and the reference values was found. It was shown that the anisotropic nature of fibrous reinforcements can be captured more appropriately by the new approach than by the isotropic FV state of the art approach, especially if high pressure gradients in the fiber direction are involved. The new model is observed to be more stable, since accounting for the anisotropic nature of the fiber reinforcements limits the distortion tendency of the mesh because deformations occur mainly in the thickness direction of the fiber reinforcements, where they are physically reasoned. Nevertheless, for more complex geometries mesh distortions can still occur as the fiber volume fraction (FVF) is updated in each cell depending on the mesh deformations but not yet transported over cell boundaries.

Fiber deformations can be captured in a homogenized form with the presented approach due to the internal coupling of fluid flow and solid deformation via Terzaghi's law. However, high local pressure gradients can lead to excessive deformation of the mesh and termination of the simulation. Therefore, a further development is necessary in future work to describe the reinforcement deformation with an Euler approach and decouple it from the mesh deformation. This is also necessary to model the new formation of pure fluid zones during infiltration. Although interfaces between porous medium and free fluid zones are already supported by the approach, the formation of new pure fluid zones cannot be captured. The proposed methods offer a profound basis from which the complexity can be further increased.

Yet a limitation of the approach is, that for materials with high anisotropy the stiffness tensor is poorly conditioned which may lead to high computational times for larger or more complex geometries. The material properties can be defined globally and rotated depending on fiber orientation and scaled to local FVF, allowing for different local fiber orientations and contents. However, due to shearing of fabrics or stacking of different materials, it could be interesting to allow for different global material properties in different model zones and skew local material coordinate systems, which is planned as next step in the model evolution.

## CRediT authorship contribution statement

Sarah Schlegel: Writing – review & editing, Writing – original draft, Visualization, Validation, Software, Methodology, Investigation, Conceptualization. **Florian Wittemann:** Writing – review & editing, Supervision, Software. **Luise Kärger:** Writing – review & editing, Supervision, Resources, Project administration, Funding acquisition.

## Declaration of competing interest

The authors declare the following financial interests/personal relationships which may be considered as potential competing interests: Luise Kärger is associate editor of Composites B. The other authors declare that they have no known competing financial interests or personal relationships that could have appeared to influence the work reported in this paper.

Acknowledgments
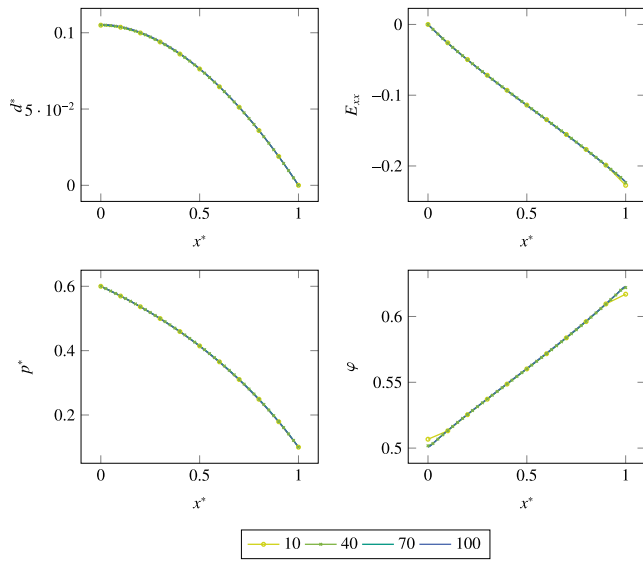
Fig. 11. Comparison of four different mesh densities of the internal coupling verification case along the normalized deformed state of the porous medium x^*: Normalized displacement d^*, component E_{xx} of Green–Lagrange strain tensor, normalized pressure p^*, and FVF φ from top left to bottom right.
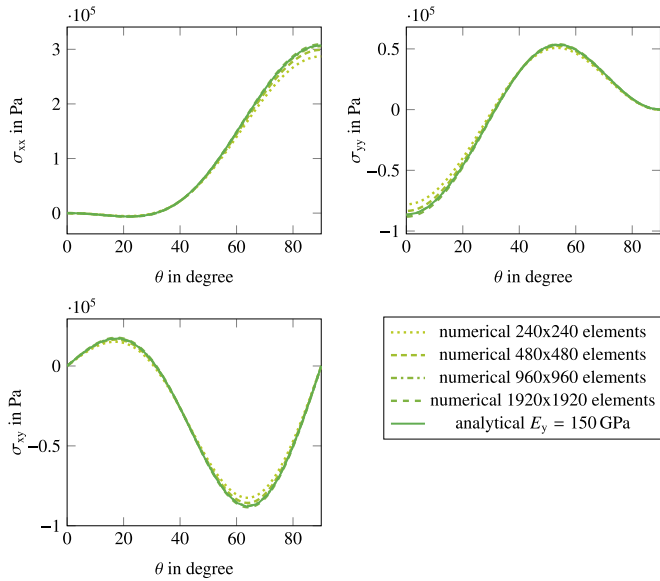
Fig. 12. Comparison of the resulting stresses at the circular cutout over the angle in an open-hole-tension verification case for four different mesh densities against the analytical solution with $E_y = 150\,\text{GPa}$.

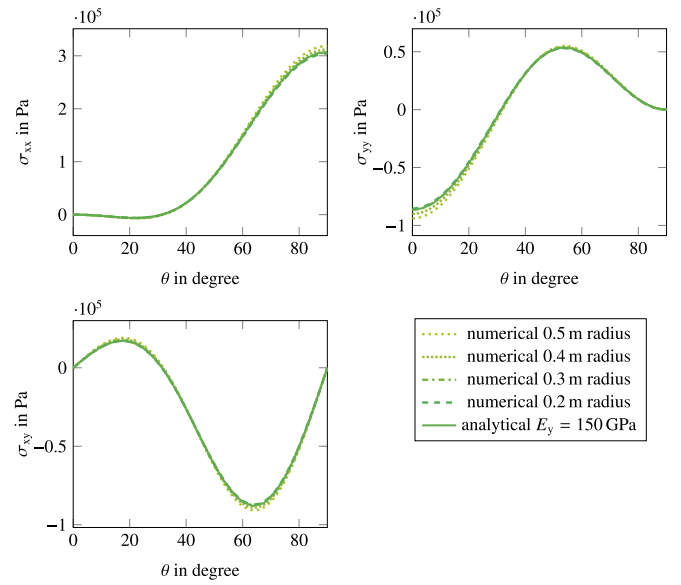# Appendix A. Mesh density study for the 1D porous solid mechanics verification

See Fig. 11.

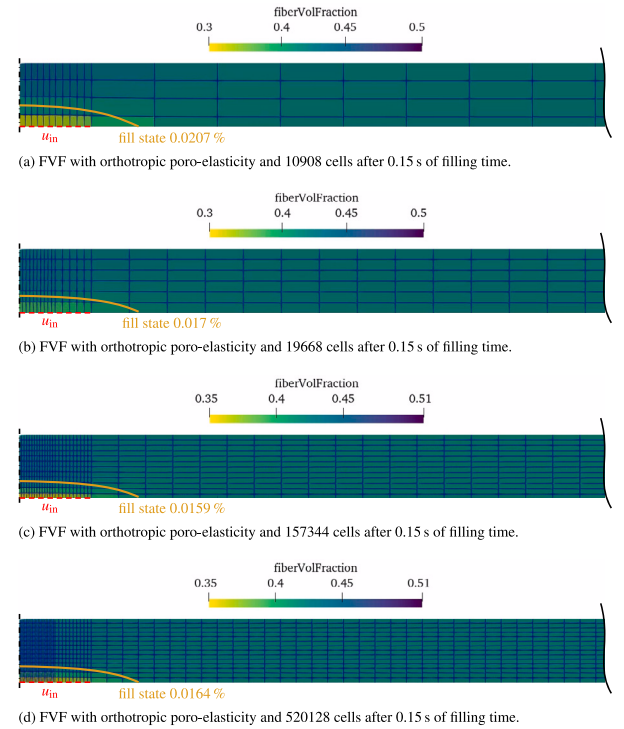# Appendix B. Mesh density study for the 2D orthotropic solid mechanics verification

See Figs. 12 and 13.

Appendix C. Mesh sensitivity study for the 3D validation case

See Fig. 14.

Fig. 13. Comparison of the resulting stresses at the circular cutout over the angle in an open-hole-tension verification case for different sizes of the cutout in a fixed size plate against the analytical solution with $E_y = 150\,\text{GPa}$.

(a) FVF with orthotropic poro-elasticity and 10908 cells after 0.15 s of filling time.

(b) FVF with orthotropic poro-elasticity and 19668 cells after 0.15 s of filling time.

(c) FVF with orthotropic poro-elasticity and 157344 cells after 0.15 s of filling time.

(d) FVF with orthotropic poro-elasticity and 520128 cells after 0.15 s of filling time.

Fig. 14. Comparison of FVF distribution near the inlet in a three-dimensional plate with four different mesh densities ((a) 10908 cells, (b) 19668 cells (chosen), (c) 157344 cells, and (d) 520128 cells). Analogously to Fig. 10, the symmetry of the plate at the center line is used to better represent the behavior at the inlet and the plate is cut off towards the edge. The inlet is indicated in red and the flow front at the given time in orange. (For interpretation of the references to color in this figure legend, the reader is referred to the web version of this article.)

Data availability

No data was used for the research described in the article.

References

[1] Lin RJ, Lee LJ, Liou MJ. Mold filling and curing analysis in liquid composite molding. Polym Compos 1993;14(1):71–81. http://dx.doi.org/10.1002/pc.750104011.

[2] Um MK, Lee WI. A study on permeability of unidirectional fiber beds. J Reinf Plast Compos 1997;1575–90.

[3] Simacek P, Advani SG. A numerical model to predict fiber tow saturation during liquid composite molding. Compos Sci Technol 2003;63(12):1725–36. http://dx.doi.org/10.1016/S0266-3538(03)00155-6.

[4] Simacek P, Advani SG. Desirable features in mold filling simulations for liquid composite molding processes. Polym Compos 2004;25(4):355–67. http://dx.doi.org/10.1002/pc.20029.

[5] Tan H, Pillai KM. Multiscale modeling of unsaturated flow in dual-scale fiber preforms of liquid composite molding I: Isothermal flows. Compos Part A: Appl Sci Manuf 2012;43(1):1–13. http://dx.doi.org/10.1016/j.compositesa.2010.12.013.

[6] Sun X, Li S, Lee L. Mold filling analysis in vacuum-assisted resin transfer molding. Part I: SCRIMP based on a high-permeable medium. Polym Compos 1998;19(6):807–17. http://dx.doi.org/10.1002/pc.10155.

[7] Hammami A, Gebart BR. Analysis of the vacuum infusion molding process. Polym Compos 2000;21(1):28–40. http://dx.doi.org/10.1002/pc.10162.

[8] Correia NC, Robitaille F, Long AC, Rudd CD, Šimáček P, Advani SG. Analysis of the vacuum infusion moulding process: I. Analytical formulation. Compos Part A: Appl Sci Manuf 2005;36(12):1645–56. http://dx.doi.org/10.1016/j.compositesa.2005.03.019.

[9] Celle P, Drapier S, Bergheau J-M. Numerical modelling of liquid infusion into fibrous media undergoing compaction. Eur J Mech A Solids 2008;27(4):647–61. http://dx.doi.org/10.1016/j.euromechsol.2007.11.002.

[10] Park CH, Saouab A. Analytical modeling of composite molding by resin infusion with flexible tooling: VARI and RFI processes. J Compos Mater 2009;43(18):1877–900. http://dx.doi.org/10.1177/0021998309341848.

[11] Al-Hamdan A, Rudd CD, Long AC. Dynamic core movements during liquid moulding of sandwich structures. Compos Part A: Appl Sci Manuf 1998;29(3):273–82. http://dx.doi.org/10.1016/S1359-835X(97)00082-1.

[12] Binetruy C, Advani SG. Foam core deformation during liquid molding of sandwich structures: Modeling and experimental analysis. J Sandw Struct Mater 2003;5(4):351–75. http://dx.doi.org/10.1177/109963603027909.

[13] Deleglise M, Binetruy C, Krawczak P. Simulation of LCM processes involving induced or forced deformations. Compos Part A: Appl Sci Manuf 2006;37(6):874–80. http://dx.doi.org/10.1016/j.compositesa.2005.04.005.

[14] Seuffert J. Mold-filling simulation of resin transfer molding with fluid-structure interaction [Doctoral thesis], Karlsruhe: Karlsruher Institut für Technologie (KIT); 2022, http://dx.doi.org/10.5445/IR/1000144393.

[15] Pillai KM, Tucker CL, Phelan FR. Numerical simulation of injection/compression liquid composite molding. Part 2: Preform compression. Compos Part A: Appl Sci Manuf 2001;32(2):207–20. http://dx.doi.org/10.1016/S1359-835X(00)00137-8.

[16] Bickerton S, Abdullah MZ. Modeling and evaluation of the filling stage of injection/compression moulding. Compos Sci Technol 2003;63(10):1359–75. http://dx.doi.org/10.1016/S0266-3538(03)00022-8.

[17] Bhat P, Merotte J, Simacek P, Advani SG. Process analysis of compression resin transfer molding. Compos Part A: Appl Sci Manuf 2009;40(4):431–41. http://dx.doi.org/10.1016/j.compositesa.2009.01.006.

[18] Merotte J, Simacek P, Advani SG. Resin flow analysis with fiber preform deformation in through thickness direction during compression resin transfer molding. Compos Part A: Appl Sci Manuf 2010;41(7):881–7. http://dx.doi.org/10.1016/j.compositesa.2010.03.001.

[19] Martin FA, Warrior NA, Simacek P, Advani S, Hughes A, Darlington R, et al. Simulation and validation of injection-compression filling stage of liquid moulding with fast curing resins. Appl Compos Mater 2018;19(4):487. http://dx.doi.org/10.1007/s10443-018-9682-4.

[20] Yang B, Jin T, Li J, Bi F. Three-dimensional numerical simulation of mold filling process in compression resin transfer molding. Appl Compos Mater 2015;22(2):209–30. http://dx.doi.org/10.1007/s10443-014-9402-7.

[21] Shojaei A. Numerical simulation of three-dimensional flow and analysis of filling process in compression resin transfer moulding. Compos Part A: Appl Sci Manuf 2006;37(9):1434–50. http://dx.doi.org/10.1016/j.compositesa.2005.06.021.

[22] Dereims A, Drapier S, Bergheau J-M, Luca P. 3D robust iterative coupling of Stokes, Darcy and solid mechanics for low permeability media undergoing finite strains. Finite Elem Anal Des 2014;94:1–15. http://dx.doi.org/10.1016/j.finel.2014.09.003.

[23] Terzaghi K. Erdbaumechanik Auf Bodenphysikalischer Grundlage. Leipzig: Franz Deuticke; 1925.

[24] Poppe C, Albrecht F, Krauß C, Kärger L. Towards numerical prediction of flow-induced fiber displacements during wet compression molding (WCM). ESAFORM 2021 2021. http://dx.doi.org/10.25518/esaform21.1938.

[25] Blais M, Moulin N, Liotier P-J, Drapier S. Resin infusion-based processes simulation: Coupled Stokes-Darcy flows in orthotropic preforms undergoing finite strain. Int J Mater Form 2017;10(1):43–54. http://dx.doi.org/10.1007/s12289-015-1259-2.

[26] Sarojini Narayana S, Barcenas L, Khoun L, Hubert P. Simulation and validation of 3D compression resin transfer moulding. 2022, https://nrc-publications.canada.ca/eng/view/object/?id=74a224b4-2fd7-4e6c-be71-ebc181b72eba.

[27] Magagnato D, Seuffert J, Bernath A, Kärger L, Henning F. Experimental and numerical study of the influence of integrated load transmission elements on filling behavior in resin transfer molding. Compos Struct 2018;198:135–43. http://dx.doi.org/10.1016/j.compstruct.2018.05.021.

[28] Carrillo FJ, Bourg IC. Modeling multiphase flow within and around deformable porous materials: A Darcy-Brinkman-Biot Approach. Water Resour Res 2021;57(2). http://dx.doi.org/10.1029/2020WR028734.

[29] Demirdžić I, Horman I, Martinović D. Finite volume analysis of stress and deformation in hygro-thermo-elastic orthotropic body. Comput Methods Appl Mech Engrg 2000;190(8):1221–32. http://dx.doi.org/10.1016/S0045-7825(99)00476-4.

[30] Cardiff P. Development of the finite volume method for hip joint stress analysis [Ph.D. thesis], Dublin: National University of Ireland; 2012.

[31] Tang T, Hededal O, Cardiff P. On finite volume method implementation of poro-elasto-plasticity soil model. Int J Numer Anal Methods Geomech 2015;39(13):1410–30. http://dx.doi.org/10.1002/nag.2361.

[32] Bernath A, Seuffert J, Dietrich S, Poppe N, Magagnato D, Wittemann F, et al. OF-RTM-6 – An OpenFOAM-6 extension with curing models and anisotropic permeability for usage in LCM simulations. Karlsruhe: Karlsruher Institut für Technologie (KIT); 2024, http://dx.doi.org/10.5281/ZENODO.13327698.

[33] Weller HG, Tabor G, Jasak H, Fureby C. A tensorial approach to computational continuum mechanics using object-oriented techniques. Comput Methods Appl Mech Engrg 1998;12(6):620. http://dx.doi.org/10.1063/1.168744.

[34] Hirt WD, Nichols BD. Volume of fluid (VOF) method for the dynamics of free boundaries. J Comput Phys 1981;39:201–25.

[35] Seuffert J, Kärger L, Henning F. Simulating mold filling in compression resin transfer molding (CRTM) using a three-dimensional finite-volume formulation. J Compos Sci 2018;2(2):23. http://dx.doi.org/10.3390/jcs2020023.

[36] Whitaker S. The Forchheimer equation: A theoretical development. Transp Porous Media 1996;25(1):27–61. http://dx.doi.org/10.1007/BF00141261.

[37] Darcy H. Les Fontaines Publiques de La Ville de Dijon. Paris: Dalmont; 1856.

[38] Whitaker S. Flow in porous media I: A theoretical derivation of Darcy's law. Transp Porous Media 1986;1:3–25.

[39] Ferziger JH, Perić M. Computational methods for fluid dynamics. 3rd ed.. Berlin, Heidelberg; s.l.: Springer Berlin Heidelberg; 2002, http://dx.doi.org/10.1007/978-3-642-56026-2.

[40] Jasak H. Dynamic mesh handling in OpenFOAM. In: 47th AIAA aerospace sciences meeting including the new horizons forum and aerospace exposition. 2009.

[41] Demirdžić I, Perić M. Space conservation law in finite volume calculations of fluid flow. Internat J Numer Methods Fluids 1988;8:1037–50.

[42] Cardiff P, Demirdžić I. Thirty years of the finite volume method for solid mechanics. Arch Comput Methods Eng 2021;109(3):331. http://dx.doi.org/10.1007/s11831-020-09523-0.

[43] Cardiff P, Tuković Ž. Solids4foam. 2021, https://bitbucket.org/philip_cardiff/solids4foam-release/src/master/.

[44] Cardiff P, Tuković Ž, Jaeger PD, Clancy M, Ivanković A. A Lagrangian cell-centred finite volume method for metal forming simulation. Internat J Numer Methods Engrg 2017;109(13):1777–803. http://dx.doi.org/10.1002/nme.5345.

[45] Cardiff P, Karač A, Ivanković A. A large strain finite volume method for orthotropic bodies with general material orientations. Comput Methods Appl Mech Engrg 2014;268:318–35. http://dx.doi.org/10.1016/j.cma.2013.09.008.

[46] Maneeratana K. Development of the finite volume method for non-linear structural applications [Ph.D. thesis], London: University of London; 2000.

[47] Bathe K-J. Finite element procedures. Englewood Cliffs, NJ: Prentice Hall; 1996.

[48] Bertóti R, Böhlke T. Flow-induced anisotropic viscosity in short FRPs. Mech Adv Mater Mod Process 2017;3(1):1. http://dx.doi.org/10.1186/s40759-016-0016-7.

[49] Koay CG. On the six-dimensional orthogonal tensor representation of the rotation in three dimensions: A simplified approach. Mech Mater 2009;41(8):951–3. http://dx.doi.org/10.1016/j.mechmat.2008.12.006.

[50] Mehrabadi MM, Cowin SC, Jaric J. Six-dimensional orthogonal tensorrepresentation of the rotation about an axis in three dimensions. Int J Solids Struct 1995;32(3):439–49. http://dx.doi.org/10.1016/0020-7683(94)00112-A.

[51] Seuffert J, Rosenberg P, Kärger L, Henning F, Kothmann MH, Deinzer G. Experimental and numerical investigations of pressure-controlled resin transfer molding (PC-RTM). Adv Manuf.: Polym Compos Sci 2020;6(3):154–63. http://dx.doi.org/10.1080/20550340.2020.1805689.

[52] MacMinn CW, Dufresne ER, Wettlaufer JS. Large deformations of a soft porous material. Phys Rev Appl 2016;5(4):044020. http://dx.doi.org/10.1103/PhysRevApplied.5.044020.

[53] Gebart BR. Permeability of unidirectional reinforcements for RTM. J Compos Mater 1992;(26):1100–33.

[54] Seuffert J, Kärger L, Henning F. Resin transfer molding (RTM) of fiber-reinforced polymer sandwich parts: Mold filling simulations with fluid structure interaction. ECCOMAS Coupled Probl 2021.

[55] Lekhnitskii SG. Theory of elasticity of an anisotropic body. Moscow: MIR Publishers; 1981.

[56] Demirdžić I, Muzaferija S, Perić M. Benchmark solutions of some structural analysis problems using finite-volume method and multigrid acceleration. Internat J Numer Methods Engrg 1997;40(10):1893–908. http://dx.doi.org/10.1002/(SICI)1097-0207(19970530)40:10<1893::AID-NME146>3.0.CO;2-L.

[57] Sarojini Narayana S, Khoun L, Trudeau P, Milliken N, Hubert P. Numerical and experimental investigation of resin flow, heat transfer and cure in a 3D compression resin transfer moulding process using fast curing resin. Adv Manuf.: Polym Compos Sci 2024;10(1):2378586. http://dx.doi.org/10.1080/20550340.2024.2378586.

[58] Castro JM, Macosko CW. Studies of mold filling and curing in the reaction injection molding process. AIChE J 1982;28(2):250–60. http://dx.doi.org/10.1002/aic.690280213.